MDPI

Article

Plasticity Resource of Cast Iron at Deforming Broaching

Yakiv Nemyrovskyi [1] , **Ihor Shepelenko** [1] **and Michael Storchak** [2,*]

1   Department of Machine Operation and Repair, Central Ukrainian National Technical University,
    7 Universytetskyi Avenue, 25006 Kropyvnytskyi, Ukraine; nemirovskijakov@gmail.com (Y.N.);
    kntucpfzk@gmail.com (I.S.)
2   Institute for Machine Tools, University of Stuttgart, Holzgartenstraße 17, 70174 Stuttgart, Germany
*   Correspondence: michael.storchak@ifw.uni-stuttgart.de; Tel.: +49-711-685-83831

Abstract: The contact interaction mechanics of deformation broaching in low-plasticity materials is studied. Particular attention is paid to the study of the stress–strain state parameters and the plasticity margin in the deformation zone during the machining of gray cast iron EN-GJL-200. The stress–strain state was analyzed using a finite-element model of the deforming broaching process for each area of the deformation zone. The model parameters of the machined material were determined experimentally by compressing specimens of gray cast iron EN-GJL-200. The changes in the parameters of accumulated strain, stress tensor components, stress triaxiality ratio, hydrostatic stress, and plasticity margin at different deformation zones along the machined specimen depth are analyzed. It is shown that there is a zone of local plastic deformation in conditions of critical contact stresses. This leads to the appearance of tensile stresses that reduce the plasticity margin in the surface layer. The impact of tool geometry on the stress–strain state of the surface layer is also discussed, and recommendations for the optimal working angle of the deforming element are provided based on plasticity margin minimization.

Keywords: deforming broaching; low-plasticity material; simulation; deformation zone; non-contact zone; plasticity

1. Introduction

Increasing requirements for the operational properties of the part's working surfaces stimulate the development of various technological methods for providing the specified parameters of these parts' subsurface layers. Deforming broaching (DBR) fully refers to such methods. The DBR is the cold plastic deformation process of a workpiece [1]. During machining, the deforming broach used as a tool moves along the generating line according to the sliding kinematic scheme [1]. As a rule, the broach is equipped with one or more working deforming elements having a conical shape. When several deforming elements are used, their diameters gradually increase and exceed the initial inner diameter of the workpiece d_0 over the tightness value a. Due to the tightness a_i on each deforming element and the total tightness of the entire broach Σa_i, the workpiece dimensions and the physical and mechanical characteristics of the machined surface are changed. Machining processes using DBR are successfully used to improve the geometric characteristics of the subsurface layer [2] and the friction surface quality of machine parts [3]. During machining in the contact area of the deformation zone, the stress–strain state (SSS) of the machined material is close to full compression [1]. This provides significant plastic deformation in the surface layer of the machined workpiece. For example, after 35–40 machining cycles of plastic materials (35–40 drawing cycles using the deforming elements with tightening), the deformation in the workpiece subsurface layers can reach a value of 350–400% [1].

To assess the product's quality, processed using the DBR method, a characteristic is used that determines the micro defectiveness of the workpiece's subsurface layers-the plasticity margin [4]. Plasticity is one of the most important characteristics of the machined

part quality, especially those subject to cyclic stresses. This characteristic is determined based on studying the SSS of the surface layer and its hardening degree [5].

The study of the plasticity margin and the possibility of controlling this characteristic is especially important when processing using the DBR of products from low-plasticity materials. These materials include graphite-containing cast irons. The ability of these materials to plastic deformation is limited by the damage to the workpiece surface layer due to the exhaustion of the plasticity margin. Determining the largest permissible deformation of the machined material, which does not cause microdefects in the surface layer, is a topical problem. For parts from materials with low plasticity, such as cast iron, for example, this is especially important. It is necessary to provide a certain plasticity margin for such parts to ensure that microdefects do not arise in the subsurface layers. Thus, the limiting permissible strain of the machined material is a technological parameter that significantly affects the performance properties of the machined parts [6].

The presented research is devoted to the stress–strain state study of the workpiece surface layer from low-plasticity material processed using the DBR method. The plasticity margin of the machined material and the regularities of its change are evaluated.

2. Methods for the Determination of Plasticity Margin

The DBR process is used as a roughing and finishing hole machining operation. This process combines the processes of shaping and strain hardening [1]. Ortiz-de-Zarate et al. presented in their study a real broaching scheme that combines these processes [7]. Sheykin and colleagues studied the features of the contact interaction between the tool and the workpiece in the deformation zone [8].

The undoubted advantages of DBR machining as a finishing operation include the possibility of obtaining an optimal microrelief of the working surface with a large support length, the possibility of hardening the surface layer to a very significant depth, providing residual compressive stresses in the surface layer, as well as the possibility of maintaining the integrity of materials fibers and the absence of abrasive charging. In combination, this ensures an increase in the performance characteristics of machined parts: it increases the wear resistance of the working surface, reduces the running-in time of rubbing surfaces, and improves the working conditions of friction surfaces. In addition, the simplicity and reliability of the DBR tool design, combined carbide broaches, and the adjustment of the process itself ensure that the DBR can be successfully used not only in high-volume production but also in repair production. Grzesik presented the current state of DBR technology and showed possible machining options for internal and external surfaces. In his study, the designs of broaching machines are also presented, and the effectiveness of the DBR process is proved [9]. Experimental and model aspects of broaching, as well as the most important technological features of this machining process and their application areas, are described in the study by Arrazola et al. [10].

The DBR process is widely used in the machining of products from ductile materials [1]. At the same time, the machining of holes from low-plasticity materials, for example, cast irons, is difficult due to the lack of data on the ultimate plasticity of the machined material. Studenets with colleagues showed the presence of all-around compression conditions in the contact zone between a deforming element and a cast-iron workpiece [11]. This indicates the fundamental possibility and potentiality of cast iron product machining using the DBR method. Sheikin and colleagues clarified the interaction scheme between the tool and the machined surface during DBR under conditions of all-around compression [12]. The presence of all-around compression conditions in the contact zone of the deforming element with the workpiece increases the plasticity of the machined material and prevents its brittle fracture. Rosenberg A.M. and Rosenberg O.A. came to this conclusion based on their study of the basic regularities of the DBR process, in particular, the basic regularities of the machined material behavior in the deformation zone [1]. Subsequent studies present examples of successful machining of cast iron parts using DBR [13,14]. At the same time, a mathematical model of this process was developed. This provided an opportunity to

develop an algorithm for calculating the stresses and strains in the deformation zone of the machined material [13]. Structural changes occurring in the deformation zone of the machined material during the processing of cast iron workpieces are presented in the study [14]. González's and colleagues noted the influence of the deforming element material on the microstructure of machined workpieces [15]. This influence was estimated by determining the final grain sizes and dislocation density. The experimental studies carried out revealed the presence of microfractures in the form of peeling of the machined parts' surface layer when using DBR. Such microfractures appeared already after several deformation cycles. Bai and Tong developed a multivariate model to calculate the SSS parameters and fix the characteristics of the microstructure, in particular, the distribution of grain sizes and dislocation density [16]. The design parameters of the tool for DBR, which ensure a high quality of the machined surface, were calculated in the work of Çırak and Altan [17]. An energy analysis of the DBR process mechanics was performed by Kishawy with colleagues [18]. At the same time, the influence of the deforming element shape on the microhardness and microstructure of the cast iron product surface layer was studied. An analysis of these results showed a low deformation limit for cast iron.

The low strain limit of cast iron indicates the necessity to carefully study the processes occurring in the deformation zone. It is known that the deformation zone in the DBR process consists of a contact zone with non-contact zones adjacent to it [2,3,8]. These zones can be a place of damage accumulation and reduction in plasticity margin. A significant number of investigations are devoted to the experimental study of the regularities occurring in the deformation zone. Wang et al. developed a plasticity model of the machined material, which considers the SSS parameters and the effect of strain, strain rate, and temperature on the material flow stress [19]. Sarkar and colleagues developed a localizing gradient plasticity model. This model avoids the influence of non-deterministic errors [20]. Natkowski et al. performed the calculation of the plasticity margin, considering the surface roughness, using an analytical method [21]. The results of this calculation showed a good correlation with experimental studies. The behavior of the material during the deformation of various cast irons with different microstructures was performed by Collini et al. [22]. At the same time, three ferrite-pearlite heterogeneous matrices are considered, which represent different classes of materials in terms of strength and plasticity. The results obtained indicate the local strain distribution and damage accumulation. Similar studies were also carried out for other materials, for example, eutectoid steels after cold plastic deformation [23]. In this case, the average residual stresses in the deformation zone were about 220 MPa. During the studies of pearlitic steel machining, it was observed that there was an uneven distribution of strain over the thickness of the specimen. [24]. It has been proven that the material structure has a significant influence on its deformability.

Plasticity, as one of the main characteristics of various materials, is the subject of numerous studies. Rastellini and colleagues proposed a new fracture criterion based on triaxial stress [25]. At the same time, they studied the plasticity accumulated throughout the material history loading. An analysis of stress development during testing and plasticity studies is presented in a study by Moakhar et al. [26]. He and colleagues studied plasticity models under various multiaxial loading conditions based on the finite element method [27]. Danas and Ponte Castañeda studied the main patterns of plasticity distribution under the triaxial loading of an elastoplastic material [28]. The studies mentioned above were carried out for plastic materials.

Several studies have also focused on the plasticity of brittle materials, particularly various cast irons. Metzger and Seifert studied the inelastic behavior of gray cast iron depending on the material microstructure [29]. In continuation of these studies, they performed modeling of the cast iron metal matrix during the elastic–plastic deformation of the specimen [30]. In further studies, these authors described the typical tension-compression asymmetry for brittle materials [31] and presented numerical studies of gray cast iron behavior [32]. This made it possible to obtain the stress–strain curves using finite-element models that take into account the material microstructure. Kasvayee with colleagues paid

special attention to the measurement of local deformation during the microcracks initiation in cast iron [33]. The values of local deformations were measured by the authors around microcracks formed in the deformation process. The obtained results showed non-uniform deformation of material microlayers. A review of micromechanical failure processes modeling in nodular cast iron was carried out by Hütter et al. [34]. They established a connection between the experimental data and the data obtained by modeling the deformation process. This made it possible to classify the resulting models according to various criteria. The studies of Kasvayee et al. [35] are devoted to the study of deformation localization and cracking in cast iron. At the same time, crack initiation was found in the stress range of 280–330 MPa. Gebhardt and colleagues studied the behavior of high-alloy nodular cast iron during its deformation [36]. The authors proved that the aluminum content affects the mechanical characteristics of this cast iron type. Shepelenko et al. identified the plastic deformation of low-ductility cast iron at significant negative values of the stress triaxiality ratio [37]. The stress triaxiality ratio is widely used to evaluate their stress–strain state [38–40]. Shepelenko and colleagues developed a method for evaluating the deformation of gray cast iron EN-GJL-200 specimens together with highly plastic material, in particular with brass, copper, and lead [41]. This ensured that the ultimate strain before material fracture was achieved $\varepsilon > 80\%$.

In recent decades, much research attention has been focused on the numerical simulation of various materials' behavior under loading conditions, which leads to plastic flow and damage in the studied materials. Razanica and colleagues developed a finite element model of the material plastic flow under deformation [42]. A model for predicting the integrity of the workpiece surface machined using DBR was developed by Ortiz-de-Zarate et al. [7]. The obtained results showed quite acceptable agreement with the experimental data. Motoyama with colleagues performed a SSS analysis of a gray cast iron workpiece using a computer-aided design system [43]. The authors concluded that the developed method could predict deformation with an error of no more than 26%. A plasticity model for modeling the formation of residual stresses and evaluating the correlation between plastic deformation, grain orientation, and residual stresses in the additive manufacturing process was developed by Grilli et al. [44]. The wide possibilities of the finite element method for modeling the shaping process and optimizing process parameters are presented in a study by Zhang with colleagues [45].

Based on the published literature analysis, it can be concluded that the deforming broaching process was mainly used in the machining of ductile materials. At the same time, the machining of holes from low-plastic materials, such as cast iron, is constrained by the lack of data on the ultimate material plasticity. The stress–strain state in the contact zone of the deforming element with the cast iron workpiece, which is close to full compression conditions, prevents the brittle fracture of the machined material and ensures an increase in its plasticity [1,4,5]. Examples of cast iron parts successfully machined using the DBR method for a specific production task are known [11]. The analysis of methods for determining the plasticity margin showed that to assess the quality of the parts machined using DBR, the characteristic that determines the defectiveness of the surface layer is the plasticity margin [4] should be used. The evaluation of the plasticity margin in the subsurface layers of the machined material should be carried out based on the SSS study. In addition, it is necessary to study the factors that affect the plasticity margin during hole machining using the DBR method in workpieces from materials with low plasticity. The study of these factors was carried out in this paper using numerical analysis.

3. Materials and Methods

The study of the material plasticity margin is especially important when machining using DBR of low-plasticity materials, such as graphite-containing cast irons, in particular gray cast iron EN-GJL-200. The stress–strain state of the machined material used to estimate the plasticity margin is characterized by the plasticity diagram of this material. Considering that the machined material in the deformation zone during DBR is in an almost all-around

compression state, characterized by large negative stress triaxiality ratio values, the plasticity diagram of the material must be extended to these values. For this purpose, the plasticity diagram of gray cast iron EN-GJL-200, including the area with the high negative values of the stress triaxiality ratio $-1 \leq \eta \leq -5$, is experimentally determined [41]. Figure 1 shows this plasticity diagram.
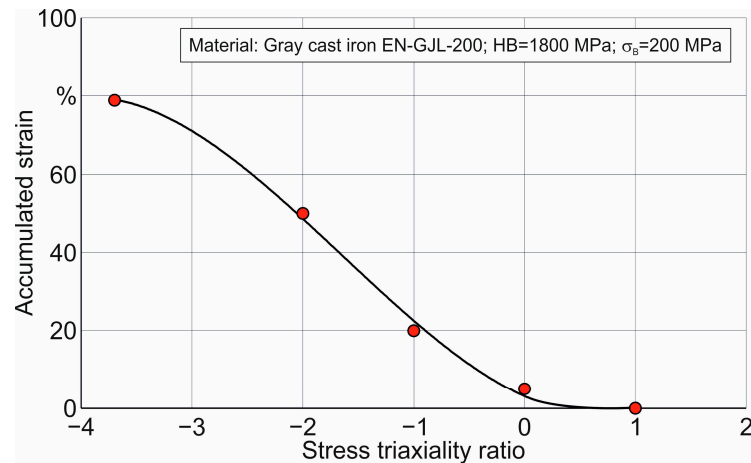

Figure 1. Plasticity diagram of cast iron EN-GJL-200.

Experimental studies were performed to determine the plasticity diagram by examining the plastic deformation process using composite samples of gray cast iron EN-GJL-200 and highly plastic materials. Brass, copper, or lead was used as highly plastic materials. The use of such composite specimens ensured that the ultimate strain before material damage was greater than 80%. Due to this, in turn, the aforementioned large negative stress triaxiality ratios were achieved. The presence of the plasticity diagram (see Figure 1) ensures the determination of the limiting technological modes during the DBR of grey cast iron EN-GJL-200 parts. In this regard, it is necessary to study the stress–strain state of the machined material in the deformation zone. In addition, it is also necessary to determine the SSS and plasticity parameters of the subsurface layers when machining with DBR. The latter will make it possible to determine the factors that affect the plasticity margin of the machined material.

The plastic shaping capabilities of gray cast iron EN-GJL-200 are limited by a significant decrease in the surface layer quality of the machined material and the subsequent damage to the workpiece subsurface layers due to the plasticity margin exhaustion of the machined material. In this case, the decrease in the quality of the surface layer is characterized by a significant increase in the roughness height parameters of the machined surface. Such a change in the roughness height parameters as a result of deforming broaching indicates the beginning of the exhaustion process of the plasticity margin from the machined material. The appearance of microfractures in the surface layer of parts machined with the DBR process negatively affects their performance properties. To avoid such phenomena, when designing the DBR process, it is necessary to ensure a positive plasticity margin of the machined material. That is, it is necessary to ensure that the permissible material plasticity exceeds the value of the plasticity margin exhaustion as a result of the deforming broaching process:

$$\psi < [\psi], \tag{1}$$

where ψ is the plasticity, exhausted as a result of the deformation; $[\psi]$ is the permissible plasticity.

Exceeding the permissible plasticity causes damage to the machined material. This damage corresponds to a certain type of material stress–strain state and corresponds to its stress triaxiality ratio value η. The permissible plasticity is determined from the plasticity diagram (see Figure 1).

3.1. Materials

Gray cast iron EN-GJL-200 (Metallurgical Plant "ArcelorMittal", Kryvyi Rih, Ukraine) was chosen as the studied low-plasticity material. The chemical composition and mechanical properties of this material are presented in Table 1.

Table 1. Chemical composition and mechanical properties of gray cast iron EN-GJL-200 [46].

Chemical Composition (%)					Mechanical Properties			
C	Cr	Si	Mn	Ti	Hardness, HB (MPa)	Strength Limit, σ_b (MPa)	Poisson's Ratio, μ	Elastic Modulus, E, (GPa)
2.65	0.10	0.1	0.5	0.08	1700–1900	200	0.27	160

The values of stress intensity σ_i and deformation intensity ε_i, characterizing the flow curve of the machined material, were determined experimentally during specimen compression. Compression test specimens were made of gray cast iron EN-GJL-200 with a diameter of 15 mm and a height of 30 mm. To reduce the friction effect between the punch surfaces and the specimen on the test results, the latter was made with end cylindrical grooves 1 mm deep and 13 mm in diameter. The groove was filled with a solid lubricant based on colloidal graphite, which allowed relatively large uniform deformations. The tests were carried out on a universal testing machine UIM-50m (Limited Liability Company "Microtest", Neftekamsk, Russia), designed to test materials for tension, compression, and bending at a maximum force of up to 500 kN. After compression testing to a certain predetermined strain value, the microhardness of the deformed specimens was measured. The microhardness measurement of specimens subjected to compression test was carried out by the method of instrumental nanoindentation [47] using the "Micron-g" device (Micron Company, Kyiv, Ukraine) [48]. Figure 2 shows the results of the compression test of gray cast iron EN-GJL-200 specimens and their microhardness measurements. The ultimate compression deformation was ε = 22%.
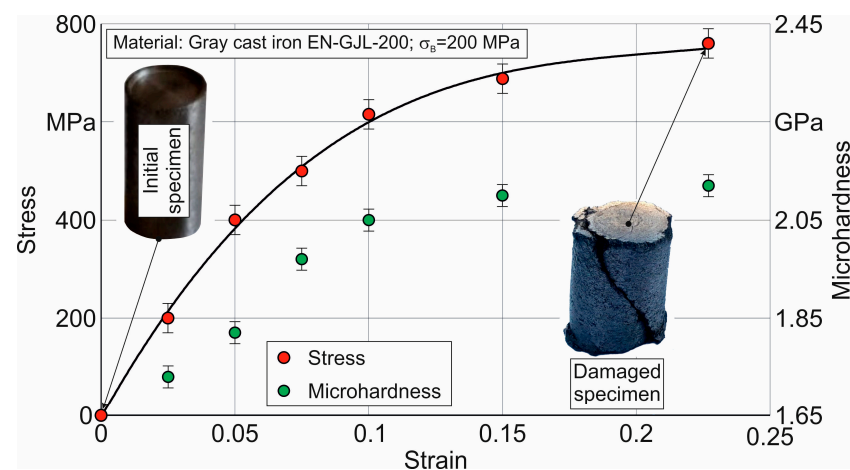

Figure 2. Flow curve of gray cast iron EN-GJL-200 with initial and damaged specimens.

The tested and measured results provided identification of the relationship between the microhardness of gray cast iron EN-GJL-200 specimens and its stress–strain state at different degrees of its deformation. This relationship is represented in Figure 3 as a dual diagram. This diagram is proposed to be used to determine the strain and/or stress value in a material through the measurement of its microhardness. In particular, it can be used when it is necessary to determine the strain or stress value in hard-to-reach places, for example, in workpieces machined using methods of plastic deformation, cutting, etc. The basic condition for using this method is the similarity (most optimally, coincidence) between

the stress–strain state of the specimens at which the dual diagram is obtained and the specimens (workpieces) in which the degree of strain and/or stress is to be determined.
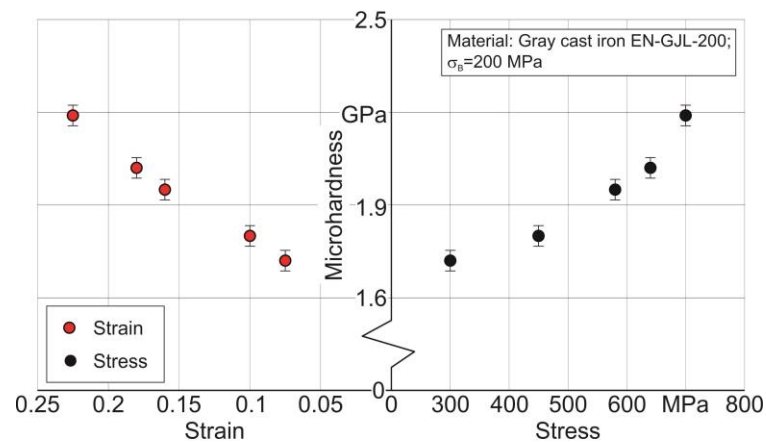

Figure 3. Correlation between the hardness of compression-tested specimens with their degree of strain and stress.

Deforming broaching of EN-GJL-200 gray cast iron bushes was performed on a 7A623 vertical broaching machine (United Joint Stock Company "Kirov Machine-Tool Plant", Minsk, Belarus). The scheme of the deforming broaching process and the deforming broach used to perform this machining process are shown in Figure 4.

(a)　　　　　　　　　　　**(b)**
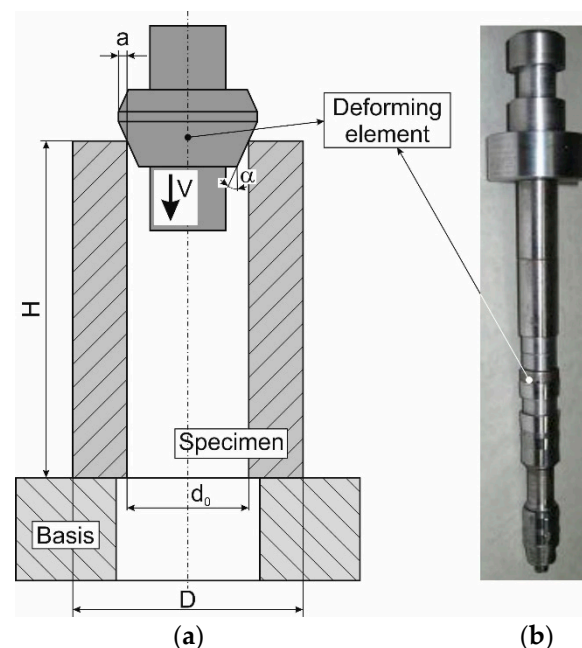
Figure 4. Deforming broaching: (**a**)—process scheme; (**b**)—deforming broach (α-generatrix inclination angle of the working cone).

Before the machining process, the working surfaces of the broach-deforming elements were polished using tools with bonded superhard materials [49,50]. The outer diameter of the workpiece (bush) was D = 55 mm, its initial inner diameter was d_0 = 35 mm, and the length of the bush was H = 80 mm. The machining speed was V = 0.5 mm/s. The deforming element tightness on each pass of the deforming broach (on each work cycle) was set equal to 0.1 mm. After each work cycle (each pass of the broach with a deforming element), the arithmetic average roughness R_a of the bush machined surface was measured. In this case, the base length was 2.5 mm. Roughness measurements were repeated at least 5 times after

each machining cycle, and then the results were averaged. The surface roughness/contour measuring system Mitutoyo Surface Roughness Tester FTA-S3000 (Mitutoyo Corporation, Neuss, Germany) was used to measure the roughness height parameters of the machined bush' surface.

The microhardness of the bush subsurface layers machined using deforming broaching was determined in the same way as the specimens subjected to the compression test. To measure microhardness, a ring was cut out from the DBR-machined bushes. The extensive cooling accompanying the cutting process ensured that the mechanical properties of the subsurface layers machined with deforming broaching were not affected when cutting was performed. Metallographic slips were prepared from the cutting rings as well as compressed specimens to measure microhardness. For this procedure, the ring as well as the specimen was placed in a silicone box filled with epoxy resin and hardener. The specimens were ground and polished with abrasive tools and pastes [49,50] after the final hardening of the composition. The thus prepared and etched surface of the slice was tested for microhardness in the depth of the subsurface layers. Nitric acid with a concentration of 3% was chosen as an etchant. The nanoindentation process for the microhardness measurement was repeated at least 7 times for each specified stress–strain state of the measured specimen. The results of the microhardness measurements obtained were averaged.

3.2. Methods

To analyze the SSS of the machined material and determine the plasticity margin, a finite element (FEM) model of the DBR process has been developed. The commercially available FEA software DEFORM 2D/3DTMV 12.0 (Version 12.0, SFTC, Columbus, OH, USA) was used for modeling [51]. The developed FEM model was applied to study the SSS of the machined material in each deformation zone during the DBR process. When modeling DBR, the same machining modes were used as in the experimental studies of the deforming broaching process: deforming element movement speed V = 0.5 mm/s, nominal tightness on the deforming element a = 0.1 mm. The DBR process modeling scheme and a fragment of the machined surface with tracking points P1, P2, and P3 in the studied deformation zone are shown in Figure 5. The specified tracking points are used to analyze the SSS in the deformation zone at different distances from the specimen surface.
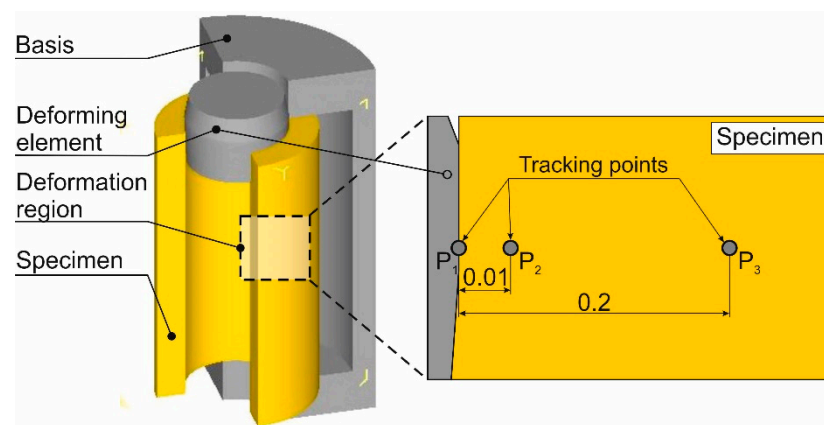

Figure 5. DBR modeling scheme.

The geometric model with mesh and boundary conditions for the simulated deforming broaching process is shown in Figure 6. The boundary conditions were set using a fixed tool (deforming element) displacement in the *x*-axis direction perpendicular to the displacement speed vector V. The displacements of the workpiece were limited in all directions. The tool working movement with the speed V was set by its absolute movement in the *y*-axis negative direction. The tightness of the deforming element was set with the value a of this element penetration into the workpiece along the *x*-axis. The workpiece dimensions, the

tightness on the deforming element, and its geometric characteristics are also shown in Figure 6.
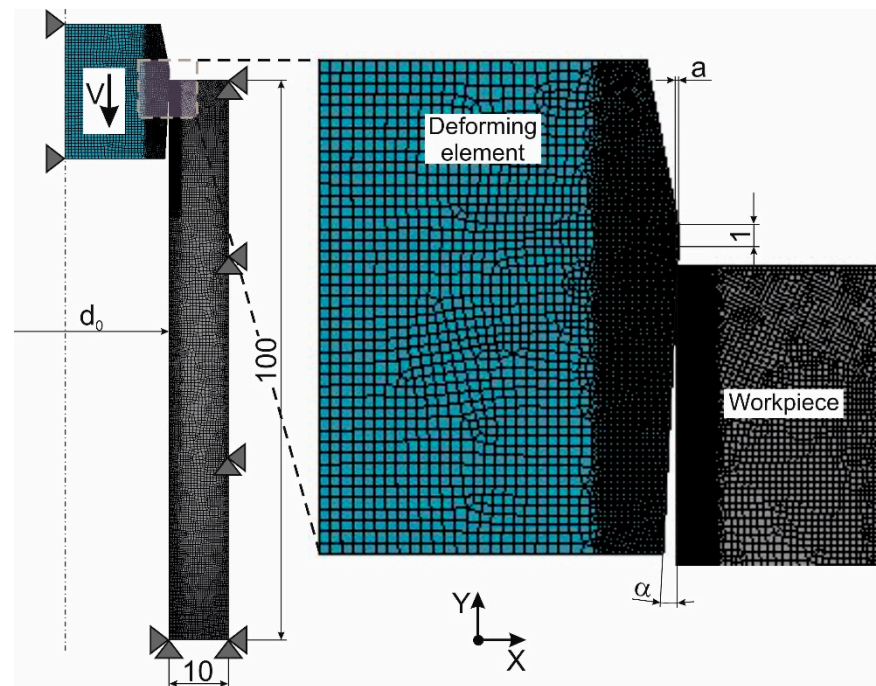

Figure 6. Initial geometry, boundary conditions, and mesh of the DBR FE-model.

The workpiece material was modeled as an isotropic plastic-type material [52]. The material model of the machined workpiece was specified in tabular form [51,53], the data for which were determined when the compression test of the specimens was performed (see Section 3.2 and Figure 2). The deforming element material was modeled as a rigid type [52,54]. The contact interaction of the deforming element with the workpiece was set by Coulomb friction. The friction coefficient during plastic deformation depends on the stress value in the contact zone of the deforming element with the workpiece [55]. Taking into account the use of protective lubricant in the deformation broaching process, the limit value of the friction coefficient is assumed to be 0.2 [1,56]. The initial workpiece model mesh contained about 20,692 elements and about 21,352 nodes. The edge length of the largest workpiece model element was about 0.443 mm, and the edge length of the smallest element was about 0.003 mm. The initial tool model mesh contained about 5055 elements and about 5203 nodes. In this case, the edge length of the largest element was about 0.512 mm, and the edge length of the smallest element was about 0.126 mm.

The machined material plasticity in the deformation zone was determined for each tracking point (see Figure 5) using the following criterion [4]:

$$\Psi = \int_0^{\varepsilon_0} \frac{1}{\varepsilon_{ul}(\eta)} \, d\varepsilon_0, \tag{2}$$

where ε_0 is the accumulated strain; $\varepsilon_{ul}(\eta)$ is the ultimate strain of the machined material at the corresponding value of the stress triaxiality ratio η.

The stress triaxiality ratio of the machined material η was calculated using the equation [38,57,58]:

$$\eta = \frac{3 \cdot \sigma}{\sigma_0}, \tag{3}$$

where σ is the hydrostatic stress, σ_0 is the stress intensity.

Hydrostatic stress σ and stress intensity σ_0 were calculated using the following equations:

$$\sigma = \frac{\sigma_1 + \sigma_2 + \sigma_3}{3}, \tag{4}$$

$$\sigma_0 = \frac{1}{\sqrt{2}}\sqrt{(\sigma_1 - \sigma_2)^2 + (\sigma_1 - \sigma_3)^2 + (\sigma_2 - \sigma_3)^2}, \tag{5}$$

where σ_1, σ_2, σ_3 are the principal stresses.

The stress and strain components required for calculations according to Equations (2)–(5) were determined using the results of the FE-model simulation for the deforming broaching process.

4. Results and Discussion

The state of the machined subsurface layers was evaluated by changing the arithmetic average roughness R_a as a result of multiple cycles of deforming broaching. The effect of the cumulative relative strain $\Sigma a_i/d_0$ from the machined material on the arithmetic average roughness R_a is shown in Figure 7.
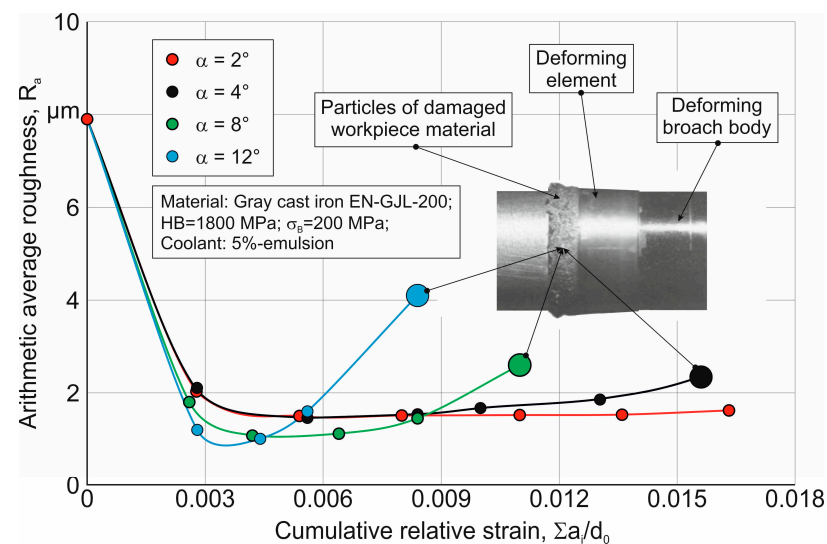

Figure 7. Effect of cumulative relative strain on the arithmetic average roughness R_a.

The measured roughness of the machined surfaces is decreased in the initial deformation cycles. In subsequent strain cycles (with a further increase in the accumulated relative strain), the measured value of R_a increases significantly. This increase in the height of microroughness is particularly significant when using deforming elements with angles $\alpha > 4°$. Additionally, the increase in the R_a parameter for deforming elements with an angle $\alpha = 12°$ appears earlier than when using deforming elements with an angle $\alpha = 8°$. The only exception is the change in roughness for deforming elements with an angle of $\alpha = 2°$. When using deforming elements with an angle $\alpha = 4°$, the increase in R_a value begins after a significant number of deformation cycles. The significant increase in roughness is caused as a result of the micro-fracture that occurs on the machined surfaces. The presence of fractured and detached particles of the machined material on the deforming element indicates the occurrence of such damage to the deformed surface (see the photo of the broach fragment with the deforming element in Figure 7). Presumably, the observed microfracture of machined surfaces is caused by brittle damage to the machined material as a result of its multiple deformations due to the exhaustion of its plasticity margin. Moreover, the onset of surface microfractures correlates well with the degree of its accumulated deformation. This is confirmed by the occurrence of machined surface damage first when using deforming elements with the angle $\alpha = 12°$, then deforming elements with the angle $\alpha = 8°$ and only

then with the angle $\alpha = 4°$. Thus, the plasticity margin exhaustion of the machined material occurs at the highest strain degree of the deformed surface.

The strain value of the workpiece surface machined with DBR was determined using the dual diagram (see Figure 3). It was assumed that the type of the stress–strain state in which the dual diagram was obtained corresponds to this state type of the machined material during deforming broaching. In other words, it was assumed that the stress–strain state of the machined material in the DBR process and the specimen compression process is uniform. Initially, the microhardness of the machined surfaces was measured by their depth, as described in Section 3.1. To evaluate the microhardness at the depth of the deformed layer equal to 0, these measurements were performed directly on the inner cylindrical surface of the machined bush with a diameter d_0. The microhardness value was used to determine the accumulated strain for different deformed layer depths of the machined material. For this purpose, the left part of the dual diagram was used (see Figure 3). Figure 8 shows the resulting variation in the accumulated strain along the depth of the deformed layer. The accumulated strain variation along the deformed layer depth of the bush machined using DBR is characterized by two regions. The first region, whose depth of the deformed layer lies from the inner cylindrical surface of the workpiece to a value equal to about 0.21 mm, is characterized by a significant accumulated strain value. With increasing the depth of the deformed layer in the first region, the accumulated strain decreases insignificantly from a value of about 0.21 on the inner surface of the workpiece to about 0.18 at a deformed layer depth of 0.2 mm. The second region is characterized by a significant decrease in the accumulated strain to zero at a deformed layer depth of about 0.4 mm. At this depth, the microhardness of the machined material is equal to the initial workpiece hardness. The values of the accumulated strain change along the deformed layer depth of the machined material obtained using the described method were further used for comparison with the simulation results of the deforming broaching process.
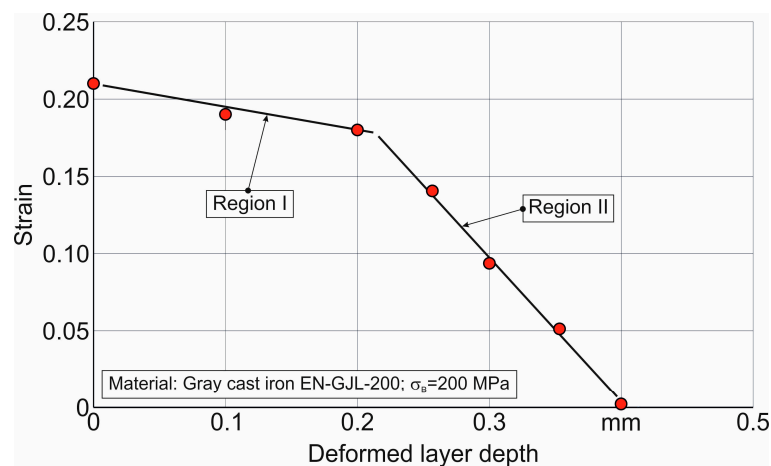

Figure 8. Strain variation along the depth of the deformed layer.

The developed finite-element model of the DBR process (see Section 3.2, Figures 5 and 6) was used to analyze the stress–strain state characteristics of the machined material in the deformation zones. As an example, two characteristics are shown in Figure 9: accumulated deformation distribution ε_0 (see Figure 9a) and stress intensity σ_0 in the specimen (see Figure 9b). Based on the simulation, the main characteristics of the stress–strain state of the machined material occurring in the deformation zones are considered and analyzed. Such characteristics include accumulated strain, the axial component of the stress tensor, stress triaxiality factor, hydrostatic stress, and plasticity characteristics, including plasticity margin and plasticity increment. The behavior of these characteristics is analyzed in the non-contact and contact zones of interaction between the deforming element and the workpiece.
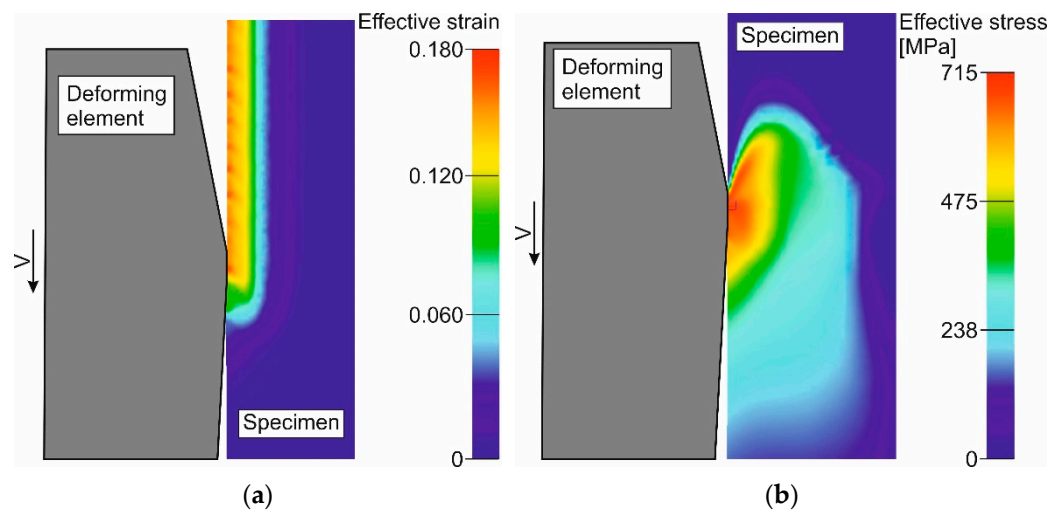
Figure 9. The distributions of accumulated strain ε_0 and stress intensity σ_0 in the machined workpiece: (**a**) distributions of accumulated strain, (**b**) stress intensity.

The accumulated strain ε_0 variation and the axial component of the stress tensor σ_z, depending on the tracking point coordinate-L and, respectively, along the machined surface length of the workpiece, are shown in Figure 10.
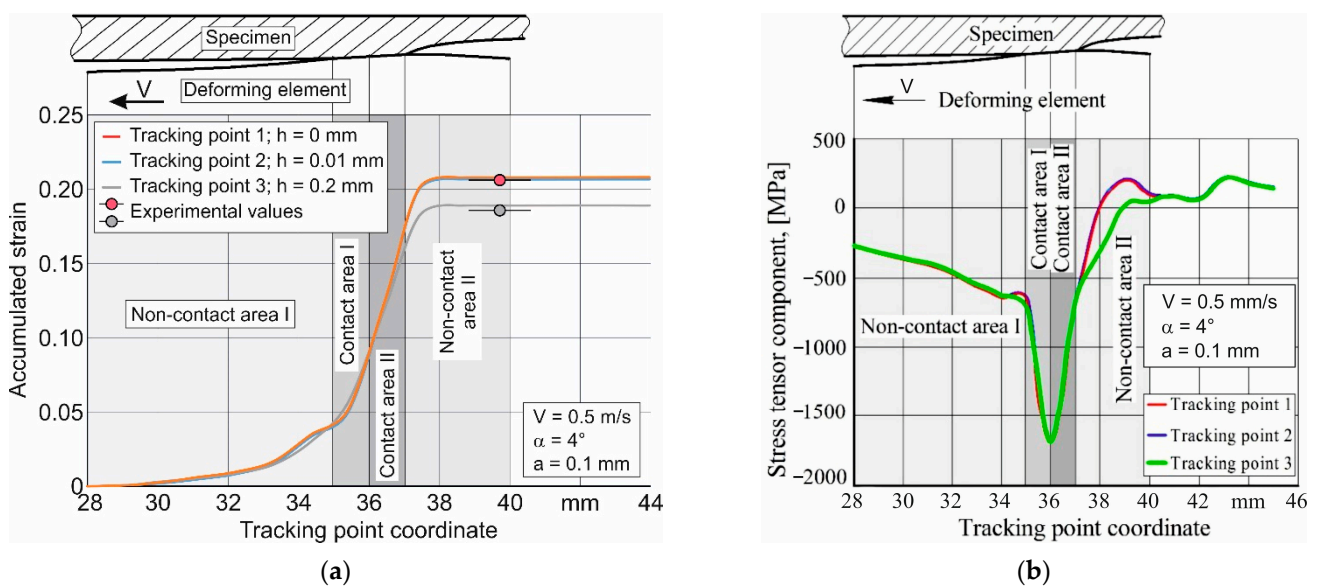

Figure 10. Dependence of the accumulated strain ε_0 and the axial component of the stress tensor σ_z on the tracking point coordinate: (**a**) accumulated strain, (**b**) axial component of the stress tensor.

The accumulated strain increases insignificantly within the non-contact zone I to a value of about 0.04, as shown in Figure 10a. In contact zones I and II, there is a significant increase in the accumulated strain to a value of about 0.16–0.17. After the machining cycle is finished, the accumulated strain reaches a certain constant value (see Figure 10a, non-contact zone II, starting from the coordinate about 38 mm), which depends on the depth coordinate of the deformed bush layer (on the distance between the inner cylindrical surface of the workpiece and the point where the strain value is determined). These accumulated strain values were also determined experimentally (see Figure 8) through the microhardness measurements along the deformed layer depth of the bush and using the dual diagram (see Figure 3). The experimental values of the accumulated strain on the bush cylindrical surface (at the depth of the deformed layer equal to 0—Figure 8) and at a distance of 0.2 mm from the machined surface (Figure 8) are plotted on the diagrams of the simulated

accumulated strain (see Figure 10a) corresponding to the distance from the machined surface. Comparison of the experimental and simulated values of the accumulated strain at the corresponding points along the deformed layer depth show their good coincidence. This provides evidence of the adequacy of the developed FE model of the deforming broaching process and the possibility to analyze other simulated characteristics of this studied process. The axial component of the stress tensor in the non-contact zone I increases smoothly in absolute value, reaching a value of about −600 MPa, as shown in Figure 10b. In contact zones I and II, the behavior of this characteristic changes dramatically. In contact zone I, the axial component of the stress tensor increases sharply in absolute value up to its maximum of about −1700 MPa. Additionally, then in contact zone II, this characteristic drastically decreases in absolute value, reaching a value of about −550 MPa. In non-contact zone II, the axial stress continues to decrease. By the end of the non-contact zone II, this characteristic takes on a relatively constant value, ranging from 100 MPa to 200 MPa.

The behavior of the stress triaxiality ratio η and hydrostatic stress σ along the machined surface length of the workpiece depending on the tracking point coordinate is presented in Figure 11. The shape of these characteristics change coincides in a certain way with the shape of the change in the axial component of the stress tensor discussed above.
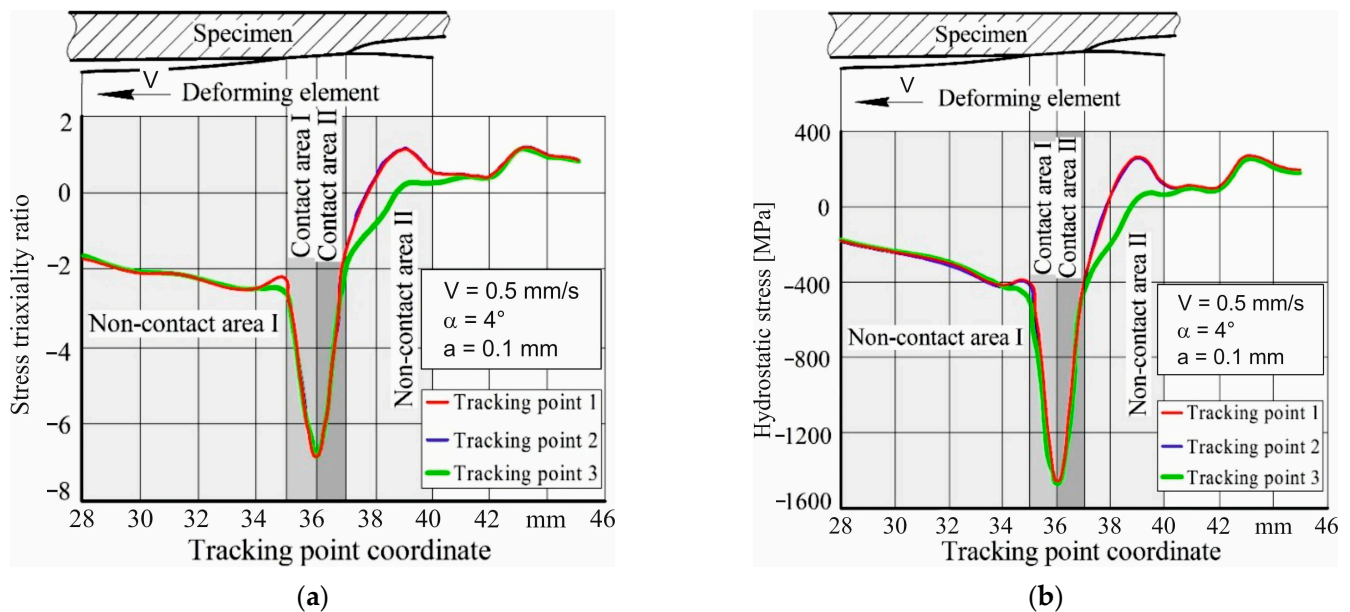

(**a**)

(**b**)

Figure 11. Change in the stress triaxiality ratio η and hydrostatic stress σ along with the tracking point coordinate. (**a**) stress triaxiality ratio, (**b**) hydrostatic stress.

The stress triaxiality ratio η in the non-contact zone I changes insignificantly, starting from a value of about η = −2.2, as shown in Figure 11a. At the end of this zone (tracking point coordinate L = 35 mm), this characteristic takes on a value of about η = −1.73. Such values of the stress triaxiality ratio η correspond to the stress state of compression under plane deformation conditions. This stress state is characterized by the presence of hydrostatic stress negative value equal to σ = −400 MPa at the end of the non-contact zone I, as shown in Figure 11b. At the same time, the above-considered stress–strain state characteristics of the machined material: the accumulated strain and the axial component of the stress tensor also change insignificantly in this zone. Thus, it is possible to define the non-contact zone I as a zone in which the characteristics of the stress–strain state of the machined workpiece surface layers are practically independent of the tracking point distance from its surface. Another SSS is observed in the transition from the non-contact zone I to the contact zone I (L ≈ 35 mm). In this case, the hydrostatic stress sharply increases in absolute value from σ ≈ −500 MPa (L ≈ 35 mm) to σ ≈ −1450 MPa (L ≈ 36 mm), as shown in Figure 11b. In turn, the negative value of the stress triaxiality ratio also increases in absolute value to

the value η = −7 (L ≈ 36 mm), as shown in Figure 11a. This indicates the transition of the material state in contact zone I into a state of powerful all-around compression. The formation of such a machined material state is also confirmed by a significant increase in the accumulated strain and the axial compressive stresses in this zone. The presence of all-around volumetric compression causes the absence of microdefects growth due to their healing. The absence of microdefect growth leads to a slight increase in the plasticity margin and a plasticity increase in contact zone I. Features of the deformation processes in the contact zone I provide an opportunity for the implementation of intense shear deformation in the subsurface layer due to friction forces. The values of the stress–strain state considered characteristics of the machined surface layers in this area are practically independent of the tracking points' distance from the workpiece surface.

Contact zone II is characterized by a significant decrease in both stress triaxiality ratio and hydrostatic stress in absolute value (see Figure 11). Thus, the stress triaxiality ratio decreases in absolute value in this zone to a value of approximately η ≈ −2, with the tracking point coordinate equal to L = 37 mm (see Figure 11a). At the same time, the hydrostatic stress also decreases in absolute value in this zone to a value approximately equal to σ ≈ −400 MPa, with the tracking point coordinate equal to L ≈ 37 mm (see Figure 11b). With further movement of the tracking point and its transition into the non-contact zone II (L = 36–40 mm), the stress triaxiality ratio and hydrostatic stress continue to decrease further in absolute value. Then, these characteristics slightly increase and take on positive values and, thereafter, remain approximately constant. The stress triaxiality ratio for tracking points P1 and P2 acquires the value η = +1 and, for tracking point P3 acquires the value—η = +0.5. The hydrostatic stress becomes a positive value and increases to the σ = 220 MPa for tracing points P1 and P2. In this case, the distance of the tracking points from the workpiece surface begins to affect the hydrostatic stress σ (see Figure 11b). This indicates the presence of a local plastic deformation zone in this area. The presence of such a zone leads to the appearance of axial tensile stresses.

It should be noted that a change in the hydrostatic stress values in contact zones I and II (Figure 11b) leads to an uneven distribution of contact loads over the total contact area between the tool and the workpiece. The hydrostatic stress variation in the contact zone determines the contact normal loads. The distribution of these loads over the contact area of the tool with the workpiece repeats the nature of the hydrostatic stress change and can be determined from Figure 11b. Thus, it can be assumed that the largest contact normal load q_k will be observed at the beginning of contact zone I, and then its value will monotonically decrease to a certain minimum. This minimum will correspond to the transition boundary of contact zone II to non-contact zone II. These changes in the contact load along the contact area between the tool and the machined surface must be taken into account in the calculation of the deforming element for strength.

The behavior of the plasticity margin ψ and plasticity increment Δψ along the length of the workpiece machined surface, depending on the tracking point coordinate, is shown in Figure 12. In non-contact zone I, a slight increase in the plasticity margin (see Figure 12a) and plasticity increment (see Figure 12b) is observed. A slight increase in the pointed characteristics of the stress–strain state of the machined material also takes place in contact zone I. In contact zone II, a sharp increase in both the plasticity margin and plasticity increment occurs. In non-contact zone II, there is a slight increase in the plasticity margin, which then takes on a constant value. At the same time, the plasticity increment decreases sharply in the non-contact zone II and remains constant at zero. In general, the behavior of the plasticity margin is similar in form to the behavior of the accumulated strain, and the behavior of the plasticity increment is similar in form to the behavior of the other, previously considered, characteristics of the stress–strain state of the machined material. The previously mentioned presence of all-around volumetric compression in contact zone I, which contributes to the absence of emerging microdefects through their healing, leads to an increase in the plasticity margin and plasticity increment. At the change in volume compression conditions at the moment of traction point transition from non-contact zone

I to contact zone I, the value of plasticity margin in the tracking point P3 at L = 37 mm is $\Delta\psi \approx 0.08$. The change in volumetric compression conditions in the transition of the tracking point from the contact zone II to the non-contact zone II causes a variation in the plasticity margin, which for the tracking points P1 and P2 increases to the value $\psi = 0.23$ (see Figure 12a). This change in volumetric compression conditions causes some exhaustion of the plasticity margin to the value in the surface layer of the workpiece (tracking points P1 and P2) equal to $\Delta\psi = 0.12$ (L = 37 mm), as shown in Figure 12b. At the same time, the increment of plasticity margin at the tracking point P3 by L = 37 mm is $\Delta\psi = 0.08$. The performed studies indicate that the most dangerous area for the exhaustion of the plasticity margin $\Delta\psi$ is the surface layer (tracking point P1). Close to it in distance, and, consequently, in terms of this characteristic value, was the tracking point P2. Tracking point P3 has a much smaller characteristic increment $\Delta\psi$. Further, it decreases with increasing the distance of tracking points from the machined surface.
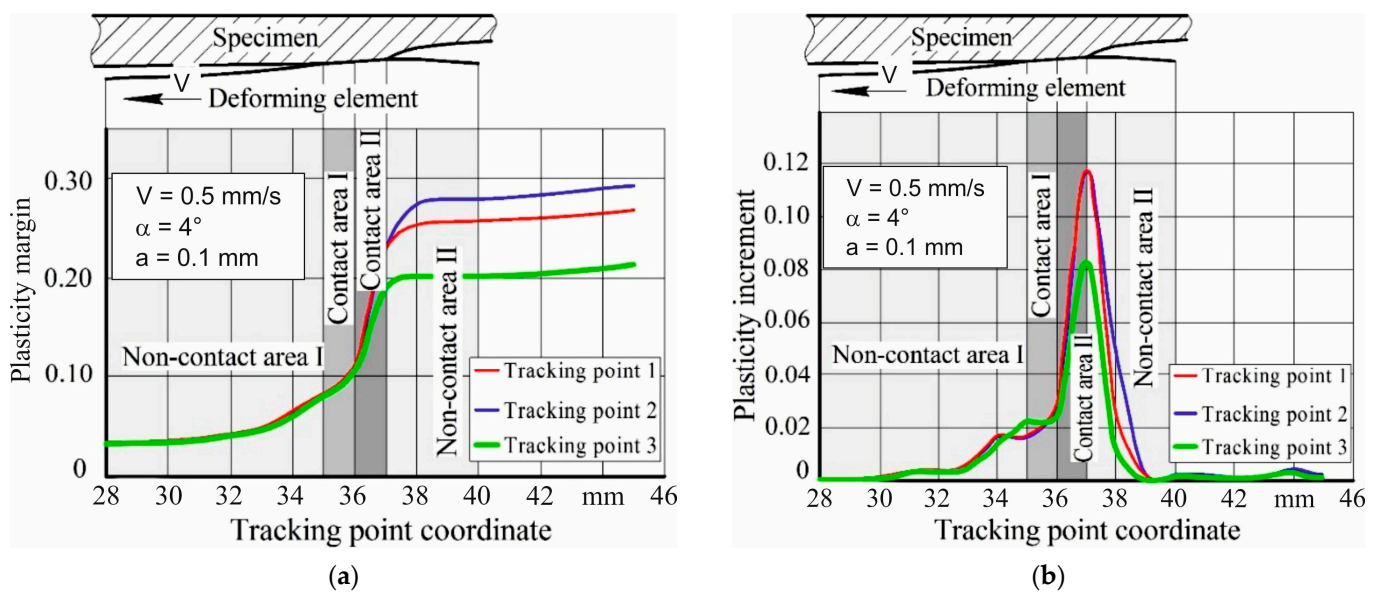

(a)   (b)

Figure 12. Dependence of plasticity margin ψ and plasticity increment $\Delta\psi$ on the tracking point coordinate. (**a**) plasticity margin, (**b**) plasticity increment.

To determine the reduction possibility of the plastic deformation local zone and thereby control the plasticity margin, the influence of the tool geometry, namely the generatrix inclination angle of the deforming element working cone α forming on the surface layer parameters, is considered. The variation in hydrostatic stress and stress triaxiality ratio along the length of the machined workpiece surface for different angles α is illustrated in Figure 13. The effect of the angle α on the plasticity margin is shown in Figure 14. The nature of changes in the values of hydrostatic stress σ, the stress triaxiality ratio η, and the plasticity margin ψ practically does not depend on the tilt angle α of the deforming element generatrix. At the same time, the angle α has a significant effect on the quantitative values of these characteristics. At the beginning of contact zone I, there is an abrupt increase in the absolute value of the hydrostatic stress from $\sigma \approx -500$ MPa to $\sigma \approx -1500$ MPa (see Figure 13a) and a corresponding increase in the absolute value of the stress triaxiality ratio η from -2 to -7 for angles $\alpha = 2°$, $4°$ and $\eta = -5$ for angle $\alpha = 12°$ (see Figure 13b). By the end of contact zone I, the hydrostatic stress σ and the stress triaxiality ratio η decrease in absolute value and even acquire positive values (see Figure 13).
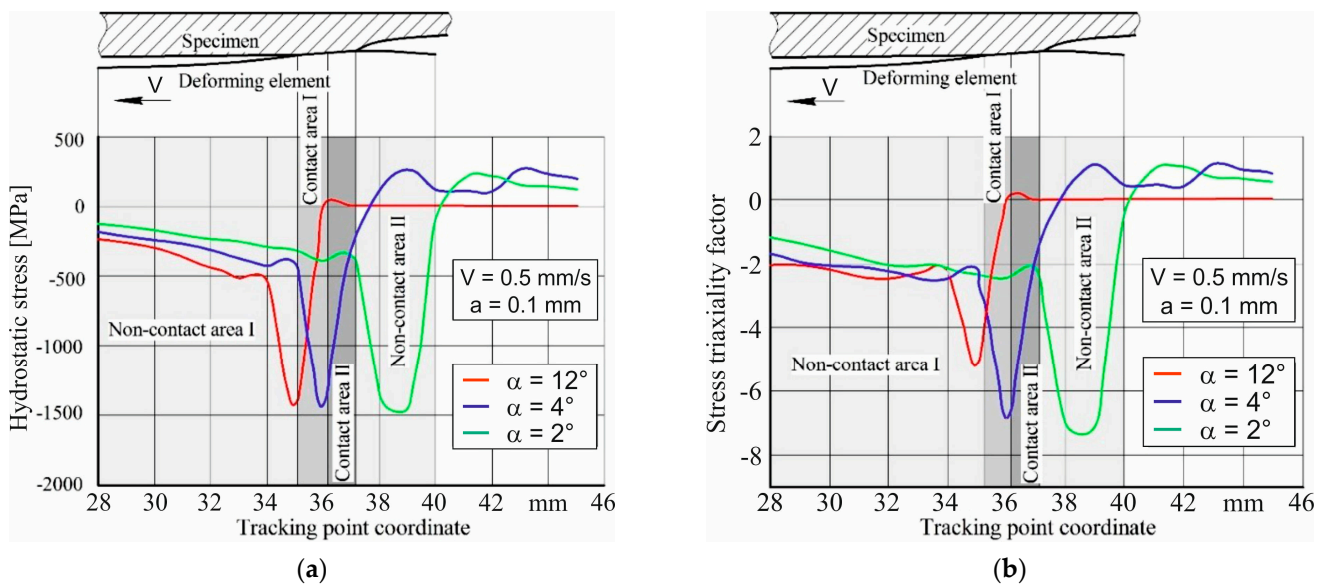
(a)

(b)

Figure 13. Dependence of hydrostatic stress σ and stress triaxiality ratio η on the tracking point coordinate. (**a**) hydrostatic stress, (**b**) stress triaxiality ratio.
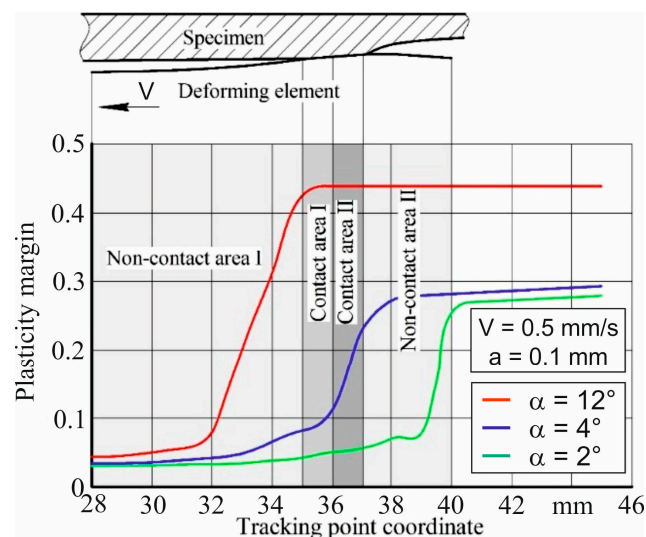

Figure 14. Dependence of the resource of plasticity ψ used on the tracking point coordinate.

This is undesirable since it leads to the exhaustion of the plasticity margin and damage to the workpiece surface layer. The plasticity margin ψ also depends on the angle α, as shown in Figure 14.

Its minimum value is reached at an angle α = 2°. This is due to the presence of the maximum negative value of the hydrostatic stress σ (see Figure 13a) and the stress triaxiality ratio η (see Figure 13b). The SSS characteristics at the moment of area transition to the non-contact zone II not only decrease their negative values but also acquire positive values for all considered values of the tilt angle α of the deforming element generatrix. This indicates the formation of a local zone of plastic deformation. The latter, in turn, leads to the exhaustion of the plasticity margin. In particular, this occurs at an angle α = 12° and leads to microfracture in the workpiece surface layer.

Thus, to ensure the high quality of the workpiece surface layer from the gray cast iron EN-GJL-200 during the DBR process, it is necessary to use the tilt angles of the deforming element generatrix no more than 4°.

5. Conclusions

The most critical area for the exhaustion of the plasticity margin is the workpiece machined surface. As the distance of tracking points from the workpiece surface increases, the plasticity margin increases.

When deforming low-plastic materials under conditions of critical contact stresses, there are zones of local plastic deformation at the beginning and the end of the contact zone. Behind the contact area, the local zone of plastic deformation creates conditions for intensive exhaustion of the machined material plasticity margin.

The main exhaustion of the plasticity margin occurs in the non-contact zone II. In this zone, the machined material from a state of significant volumetric compression in contact zone II passes to less intense compression. The appearance of a stress change gradient at the interface between the contact area and the non-contact zone behind it causes a change in the stress sign. This, in turn, leads to the appearance of axial tensile stresses, which sharply increase the accumulation of microdefects in the non-contact zone. As a result of this microdefect accumulation, the plasticity margin is exhausted.

To increase the plasticity margin, it is necessary to apply the tilt angle of the tool working cone generatrix more than $4°$.

References

1. Rosenberg, A.M.; Rosenberg, O.A. *Mechanics of Plastic Deformation in the Processes of Cutting and Deforming Broaching*; Naukova Dumka: Kyiv, Ukraine, 1990; p. 320. ISBN 5-12-001624-3. (In Russian)
2. Sheykin, S.Y.; Rostotskyi, I.Y.; Protsyshyn, V.T.; Melnichenko, V.V.; Studenets, S.F.; Efrosinin, D.V. Improving the Performance of Hard-Alloy Deforming Broaches Using Modified Technological Lubricants. *J. Superhard Mater.* **2020**, *42*, 276–282. [CrossRef]
3. Bekaev, A.A.; Mikhailov, V.A.; Kuz'minskii, D.L. Influence of the hole in the blank on the quality and precision of the hole obtained by broaching. *Russ. Eng. Res.* **2011**, *31*, 362–364. [CrossRef]
4. Kolmogorov, V.L.; Spevak, L.F.; Churbayev, R.V. On the technique used to determine plasticity margin in high-speed deformation under high pressure. *Int. J. Mech. Sci.* **2008**, *50*, 676–682. [CrossRef]
5. Kolmogorov, V.L.; Fedotov, V.P.; Gorshkov, A.V. Three-dimensional analysis of the stress–strain state in the process of plastic deformation of metals. *J. Mater. Process. Technol.* **1999**, *95*, 55–64. [CrossRef]
6. Kõrgesaar, M. The effect of low stress triaxialities and deformation paths on ductile fracture simulations of large shell structures. *Mar. Struct.* **2019**, *63*, 45–64. [CrossRef]
7. Ortiz-De-Zarate, G.; Madariaga, A.; Garay, A.; Azpitarte, L.; Sacristan, I.; Cuesta, M.; Arrazola, P. Experimental and FEM analysis of surface integrity when broaching Ti64. *Procedia CIRP* **2018**, *71*, 466–471. [CrossRef]
8. Sheykin, S.Y.; Grushko, O.V.; Melnichenko, V.V.; Studenets, S.F.; Rostotskyi, I.Y.; Iefrosinin, D.V. On the Contact Interaction between Hard-Alloy Deforming Broaches and a Workpiece during the Shaping of Grooves in the Holes of Tubular Products. *J. Superhard Mater.* **2021**, *43*, 222–230. [CrossRef]
9. Grzesik, W. Development in broaching technology. Part I. Development of broaching machines and tooling devices. *Mechanik* **2021**, *5*, 6–11. [CrossRef]
10. Arrazola, P.J.; Rech, J.; M'Saoubi, R.; Axinte, D. Broaching: Cutting tools and machine tools for manufacturing high quality features in components. *CIRP Ann.—Manuf. Technol.* **2020**, *69*, 554–577. [CrossRef]

11. Studenets', S.F.; Eryomin, P.M.; Chernyavs'kyi, O.V. The influence of deformation conditions on the structure and hardening of cast iron surface layer in machining with combined carbide broaches. *J. Superhard Mater.* **2015**, *37*, 282–288. [CrossRef]

12. Sheikin, S.E.; Paschenko, E.A.; Rostotsky, I.Y.; Gavrilova, V.S.; Protsishin, V.T. Process lubricant for deforming broaching of pieces made of titanium. *Metall. Min. Ind.* **2014**, *6*, 56–65. Available online: https://library.ajman.ac.ae/eds/detail?db=asn&an=101641048 (accessed on 25 January 2023).

13. Václav, Š.; Sivtsev, N.; Senderská, K. Investigation of stress-strain state of a workpiece at gauge burnishing of its holes. *Adv. Sci. Technol. Res. J.* **2017**, *11*, 211–222. [CrossRef]

14. Chen, Z.; Peng, R.L.; Moverare, J.; Avdovic, P.; Zhou, J.M.; Johansson, S. Surface Integrity and Structural Stability of Broached Inconel 718 at High Temperatures. *Metall. Mater. Trans. A* **2020**, *47*, 3664–3676. [CrossRef]

15. González, G.; Plogmeyer, M.; Zanger, F.; Biehl, S.; Bräuer, G.; Schulze, V. Effect of tool coatings on surface grain refinement in orthogonal cutting of 4140 steel. *Procedia CIRP* **2020**, *87*, 176–180. [CrossRef]

16. Bai, J.; Tong, Z. A novel multiscale material plasticity simulation model for high-performance cutting AISI 4140 steel. *Int. J. Adv. Manuf. Technol.* **2021**, *116*, 3891–3904. [CrossRef]

17. Çırak, O.; Altan, E. Development of a Software for Designing In-Hole Broaching Tools. *J. Adv. Manuf. Eng.* **2020**, *1*, 101–121. Available online: https://dergipark.org.tr/en/pub/jame/issue/65471/1012079 (accessed on 25 January 2023).

18. Kishawy, H.A.; Hosseini, A.; Moetakef-Imani, B.; Astakhov, V.P. An energy-based analysis of broaching operation: Cutting forces and resultant surface integrity. *CIRP Ann.—Manuf. Technol.* **2012**, *61*, 107–110. [CrossRef]

19. Dou, W.; Xu, Z.; Hu, H.; Huang, H. A generalized plasticity model incorporating stress state, strain rate and temperature effects. *Int. J. Impact Eng.* **2021**, *155*, 103897. [CrossRef]

20. Sarkar, S.; Singh, I.V.; Mishra, B.K. A localizing gradient plasticity model for ductile fracture. *Comput. Methods Appl. Mech. Eng.* **2022**, *388*, 114205. [CrossRef]

21. Natkowski, E.; Sonnweber-Ribic, P.; Münstermann, S. Surface roughness influence in micromechanical fatigue lifetime prediction with crystal plasticity models for steel. *Int. J. Fatigue* **2022**, *23*, 106792. [CrossRef]

22. Collini, L.; Moroni, F.; Pirondi, A. Modeling the influence of stress triaxiality on the failure strain of nodular cast iron microstructures. *Procedia Struct. Integr.* **2019**, *18*, 671–687. [CrossRef]

23. Stashkov, A.N.; Schapova, E.A.; Afanasiev, S.V.; Stashkova, L.A.; Nichipuruk, A.P. Estimation of residual stresses in plastically deformed eutectoid steel with different perlite morphology via magnetic parameters. *J. Magn. Magn. Mater.* **2022**, *546*, 168850. [CrossRef]

24. Yajima, Y.; Koga, N.; Watanabe, C. Influential factors on the deformability of colonies in pearlitic steel. *Mater. Charact.* **2021**, *177*, 111197. [CrossRef]

25. Rastellini, F.; Socorro, G.; Forgas, A.; Onate, E. A triaxial failure diagram to predict the forming limit of 3D sheet metal parts subjected to multiaxial stresses. *J. Phys. Conf. Ser.* **2016**, *734*, 032020. [CrossRef]

26. Moakhar, S.; Hentati, H.; Barkallah, M.; Louati, J.; Haddar, M. Influence of geometry on stress state in bulk characterization tests. *Comptes Rendus Mécanique* **2019**, *347*, 930–943. [CrossRef]

27. He, X. Predicting ductility of Mg/SiCp nanocomposite under multiaxial loading conditions based on unit cell modeling. *Int. J. Mech. Sci.* **2020**, *184*, 105831. [CrossRef]

28. Danas, K.; Ponte Castañeda, P. Influence of the Lode parameter and the stress triaxiality on the failure of elasto-plastic porous materials. *Int. J. Solids Struct.* **2012**, *49*, 1325–1342. [CrossRef]

29. Metzger, M.; Seifert, T. Computational assessment of the microstructure-dependent plasticity of lamellar gray cast iron—Part I: Methods and microstructure-based models. *Int. J. Solids Struct.* **2015**, *66*, 184–193. [CrossRef]

30. Metzger, M.; Seifert, T. Computational assessment of the microstructure-dependent plasticity of lamellar gray cast iron—Part II: Initial yield surfaces and directions. *Int. J. Solids Struct.* **2015**, *66*, 194–206. [CrossRef]

31. Metzger, M.; Seifert, T. Computational assessment of the microstructure-dependent plasticity of lamellar gray cast iron—Part III: A new yield function derived from microstructure-based models. *Int. J. Solids Struct.* **2016**, *87*, 102–109. [CrossRef]

32. Metzger, M.; Seifert, T. Computational assessment of the microstructure-dependent plasticity of lamellar gray cast iron—Part IV: Assessment of the yield surface after plastic loading. *Int. J. Solids Struct.* **2018**, *141*, 173–182. [CrossRef]

33. Kasvayee, K.A.; Ghassemali, E.; Jarfors, A.E. Micro-Crack Initiation in High-Silicon Cast Iron during Tension Loading. In Proceedings of the TMS 2015 Annual Meeting & Exhibition, Orlando, FL, USA, 15–19 March 2015; pp. 947–953. [CrossRef]

34. Hütter, G.; Zybell, L.; Kuna, M. Micromechanisms of fracture in nodular cast iron: From experimental findings towards modeling strategies—A review. *Eng. Fract. Mech.* **2015**, *144*, 118–141. [CrossRef]

35. Kasvayee, K.A.; Ghassemali, E.; Salomonsson, K.; Sujakhu, S.; Castagne, S.; Jarfors, A.E. Strain localization and crack formation effects on stress-strain response of ductile iron. *Mater. Sci. Eng. A* **2017**, *702*, 265–271. [CrossRef]

36. Gebhardt, C.; Nellessen, J.; Bührig-Polaczek, A.; Broeckmann, C. Influence of Aluminum on Fatigue Strength of Solution-Strengthened Nodular Cast Iron. *Metals* **2021**, *11*, 311. [CrossRef]

37. Shepelenko, I.; Tsekhanov, Y.; Nemyrovskyi, Y.; Gutsul, V.; Mahopets, S. Compression Mechanics of Cylindrical Samples with Radial Deformation Limitation. In *Lecture Notes in Mechanical Engineering*; Advances in Design, Simulation and Manufacturing IV. DSMIE-2021; Springer: Cham, Switzerland, 2021; pp. 53–62. [CrossRef]

38. Rice, J.R.; Tracey, D.M. On the ductile enlargement of voids in triaxial stress fields. *J. Mech. Phys. Solids* **1969**, *17*, 201–217. [CrossRef]

39. Andrade, F.; de Sá, J.C.; Pires, F.A. Assessment and comparison of non-local integral models for ductile damage. *Int. J. Damage Mech.* **2014**, *23*, 261–296. [CrossRef]

40. Ammar, M.M.A.; Shirinzadeh, B.; Elgamal, H.; Nasr, M.N.A. On the Role of Damage Evolution in Finite Element Modeling of the Cutting Process and Sensing Residual Stresses. *Sensors* **2022**, *22*, 8547. [CrossRef]

41. Shepelenko, I.; Nemyrovskyi, Y.; Tsekhanov, Y.; Mirzak, V.; Mahopets, S. Features of Plasticity Diagram Construction for Low-Plastic Materials. In *Lecture Notes in Mechanical Engineering*; Advanced Manufacturing Processes III. InterPartner-2021; Springer: Cham, Switzerland, 2022; pp. 353–362. [CrossRef]

42. Razanica, S.; Malakizadi, A.; Larsson, R.; Cedergren, S.; Josefson, B.L. Fe modeling simulation Machining Alloy718 based ductile continuum damage. *Int. J. Mech. Sci.* **2020**, *171*, 105375. [CrossRef]

43. Motoyama, Y.; Sekiguchi, S.; Okane, T.; Yoshida, M. Thermo-elasto-plastic finite element analysis of warping deformation during casting of gray cast iron. *J. Mater. Process. Technol.* **2020**, *277*, 116454. [CrossRef]

44. Grilli, N.; Hu, D.; Yushu, D.; Chen, F.; Yan, W. Crystal plasticity model of residual stress in additive manufacturing using the element elimination and reactivation method. *Comput. Mech.* **2021**, *69*, 825–845. [CrossRef]

45. Zhang, X.; Zhang, Y.; Yin, Y.; Zhang, Y.; Li, S.; Duan, S.; Huang, Z.; Chen, B.; Pei, S.; Wang, H. Simulation of the forming process of conical cup shaped by laser-induced shock waves. *Int. J. Adv. Manuf. Technol.* **2017**, *91*, 1619–1630. [CrossRef]

46. Álvarez, L.; Luis, C.J.; Puertas, I. Analysis of the influence of chemical composition on the mechanical and metallurgical properties of engine cylinder blocks in grey cast iron. *J. Mater. Process. Technol.* **2004**, *153–154*, 1039–1044. [CrossRef]

47. Zakiev, I.; Storchak, M.; Gogotsi, G.A.; Zakiev, V.; Kokoieva, Y. Instrumented indentation study of materials edge chipping. *Ceram. Int.* **2021**, *47*, 29638–29645. [CrossRef]

48. Storchak, M.; Zakiev, I.; Träris, L. Mechanical properties of subsurface layers in the machining of the titanium alloy Ti10V2Fe3Al. *J. Mech. Sci. Technol.* **2018**, *32*, 315–322. [CrossRef]

49. Filatov, Y.D.; Sidorko, V.I.; Filatov, O.Y.; Yaschuk, V.P.; Heisel, U.; Storchak, M. Surface quality control in diamond abrasive finishing. *Proc. SPIE* **2009**, *7389*, 833–841. [CrossRef]

50. Filatov, Y.D.; Filatov, A.Y.; Syrota, O.O.; Yashchuk, V.P.; Monteil, G.; Heisel, U.; Storchak, M. The influence of tool wear particles scattering in the contact zone on the workpiece surface microprofile formation in polishing quartz. *J. Superhard Mater.* **2010**, *32*, 415–422. [CrossRef]

51. Fluhrer, J. *Deform-User Manual Deform V12.0*; SFTC: Columbus, OH, USA, 2019.

52. Heisel, U.; Krivoruchko, D.V.; Zaloha, W.A.; Storchak, M.; Stehle, T. Thermomechanical material models in the modeling of cutting processes. *ZWF Z. Wirtsch. Fabr.* **2009**, *104*, 482–491. [CrossRef]

53. Storchak, M.; Jiang, L.; Xu, Y.; Li, X. Finite element modeling for the cutting process of the titanium alloy Ti10V2Fe3Al. Production Engineering. *Res. Dev.* **2016**, *10*, 509–517. [CrossRef]

54. Heisel, U.; Krivoruchko, D.V.; Zaloha, W.A.; Storchak, M.; Stehle, T. Breakage models for the modeling of cutting processes. *ZWF Z. Wirtsch. Fabr.* **2009**, *104*, 330–339. [CrossRef]

55. Tsekhanov, J.; Storchak, M. Development of analytical model for orthogonal cutting. *Prod. Eng. Res. Dev.* **2015**, *9*, 247–255. [CrossRef]

56. Heisel, U.; Krivoruchko, D.V.; Zaloha, W.A.; Storchak, M.; Stehle, T. Thermomechanical exchange effects in machining. *ZWF Z. Wirtsch. Fabr.* **2009**, *104*, 263–272. [CrossRef]

57. Ogorodnikov, V.A.; Dereven'ko, I.A.; Sivak, R.I. On the Influence of Curvature of the Trajectories of Deformation of a Volume of the Material by Pressing on Its Plasticity Under the Conditions of Complex Loading. *Mater. Sci.* **2018**, *54*, 326–332. [CrossRef]

58. Yoon, S.-Y.; Barlat, F.; Lee, S.-Y.; Kim, J.-H.; Wi, M.-S.; Kim, D.-J. Finite element implementation of hydrostatic pressure-sensitive plasticity and its application to distortional hardening model and sheet metal forming simulations. *J. Mater. Process. Technol.* **2022**, *302*, 117494. [CrossRef]